VALIDATION OF SHIFT CELL APPROACH FOR THE MODELLING OF ACOUSTIC PROPERTIES OF POROUS MATERIALS EMBEDDING PERIODIC INCLUSIONS

D Magliacano, M. Ouisse, A. Khelif, S de Rosa, F Franco, Noureddine Atalla

NOVEM 2018
Noise and vibration emerging methods
The 6th conference, 7 – 9 May 2018
Ibiza – Spain

VALIDATION OF SHIFT CELL APPROACH FOR THE MODELLING OF ACOUSTIC PROPERTIES OF POROUS MATERIALS EMBEDDING PERIODIC INCLUSIONS

D. Magliacano[12*], M. Ouisse[1], A. Khelif [1], S. De Rosa[2], F. Franco[2] and N. Atalla[3]

[1]Univ. Bourgogne Franche-Comté // FEMTO-ST Institute // CNRS/UFC/ENSMM/UTBM
Department of Applied Mechanics // 25000 Besançon, FRANCE
[*]Email: dario.magliacano@univ-fcomte.fr

[2]Università degli Studi di Napoli "Federico II" (UniNa)
Corso Umberto I 40, 80138 Napoli, ITALY

[3]Université de Sherbrooke (UdeS)
2500 boul. de l'Université, Sherbrooke (Québec) J1K 2R1, CANADA

ABSTRACT

The design based on periodic elements can be a powerful strategy for the achievement of lightweight sound packages and can represent a useful solution for manufacturing aspects. The inclusion of vibroacoustic design rules, at early stage of the product development, is a feasible and interesting research target; in fact, the use of porous media with periodic inclusions can improve the dynamic filtering effects thus offering several possibilities of applications in the engineering fields where both weight and space, as well as vibroacoustic integrity and comfort, still represent critical issues. Indeed, although porous materials are commonly used for vibroacoustic applications, they suffer from a lack of absorption at low frequencies. This difficulty is usually overcome by a multi-layering approach. However, while reducing the impedance mismatch at the air-material interface, the efficiency of such devices relies on the allowable thickness. A more efficient way to enhance the low frequency performances of sound packages consists in embedding periodic inclusions in a porous layer. If the radius of these periodic inclusions is comparable with the acoustic wavelength, then an increase of the acoustical performances can be observed since the excitation of additional acoustic modes helps in dissipating more acoustic energy. Therefore, even if this procedure still relies on the dimension of the inclusions, it can provide an acoustical performance improvement, which is way more efficient than just increasing the thickness. This paper starts with the description of the shift cell technique, which allows the description of the propagation of all existing waves

from the description of the unit cell. The shift cell technique provides a reformulation of Floquet-Bloch periodic conditions and its major advantage is that it allows the implementation of any frequency dependence and damping in the problem: this is a new advantage when computing the dispersion curves of a porous material modelled as an equivalent fluid. The second part of this work shows the improvements of acoustic properties (in terms of transmission loss) that are obtained due to the periodic nature of the system and some qualitative considerations. The test case herein presented involves a square unit cell of porous material with a circular inclusion, for which the results are quite encouraging and promising.

LIST OF SYMBOLS

- $\omega =$ angular frequency;
- $x, y, z =$ space variables;
- $j =$ imaginary unit;
- $p_0 =$ amplitude of the excitation mode (incident pressure);
- $\rho_0 =$ density of the interstitial fluid (air);
- $c_0 =$ sound speed in the interstitial fluid (air);
- $Z_0 =$ characteristic impedance of the interstitial fluid (air);
- $k_0 =$ wave number in the interstitial fluid (air);
- $\rho =$ density of the material;
- $Z_c =$ characteristic impedance of the material;
- $k =$ wave number in the material;
- $p =$ pressure;
- $K =$ bulk modulus;
- $\theta, \phi =$ angles of incidence;
- $p^* = conj(p)$;
- $\Omega =$ poro-elastic volume;
- $\Gamma =$ domain boundary;
- $I =$ flow of energy;
- $E =$ total energy;
- $E_k =$ kinetic energy;
- $m =$ mass;
- $C_p =$ particle velocity;
- $C_g =$ group velocity;
- $s =$ side length;
- $\Pi_{diss} =$ total dissipated power;
- $\Pi_{therm} =$ thermal dissipated power;
- $\Pi_{visc} =$ viscous dissipated power;
- $\Pi_{inc} =$ incident power;
- $\Pi_{input} =$ input power;
- $\Pi_{trans} =$ transmitted power;
- $S =$ surface interested by incident pressure;
- $d =$ thickness;
- $\tau_\infty =$ transmission coefficient;
- $TL =$ transmission loss.

1. INTRODUCTION

The design based on the inclusion of vibroacoustic design rules at early stage of products development, through the use of porous media with periodic inclusions which exhibit proper dynamic filtering effects, is a powerful strategy for the achievement of lightweight sound packages and represents a convenient solution for manufacturing aspects.
The main advantage of designing sound packages with periodic arrangements is that they can provide a combination of absorption effects, resonance effects and wave interferences effects. This offers different applications in transportation (aeronautics, space, automotive, railway), energy and civil engineering sectors, where both weight and space, as well as vibroacoustic integrity and comfort, still remain as critical issues.
Indeed, although porous materials are commonly used for vibroacoustic applications, they suffer from a lack of absorption at low frequencies compared to their efficiency at higher ones. This difficulty is usually overcome by multi-layering. However, while reducing the impedance mismatch at the air-material interface, the efficiency of such devices relies on the allowable thickness. Instead, a more efficient way to enhance the low frequency performances of sound packages consists in embedding periodic inclusions in a porous layer. If the radius of these periodic inclusions is comparable with the acoustic wavelength, then an increase of the acoustical performances can be observed.
In order to develop efficient numerical techniques in order to handle the problem, the shift cell operator technique here is presented, providing details on its implementation [1]. Essentially, the shift cell technique consists of a reformulation of the Floquet-Bloch partial differential problem, in which the phase shift of the boundary conditions related to wave propagation is integrated into the derivation operator. Consequently, the periodicity is included in the overall behaviour of the structure while the continuity conditions are imposed at the edges of the unit cell. Its major advantage is that it allows to implement any frequency dependence and damping in the problem; this is essential, if one needs to compute the dispersion curves of a porous material modelled as an equivalent fluid. In detail, it allows the description of the propagation of all existing waves from the description of the unit cell through the resolution of a quadratic eigenvalue problem. This is done through the $k(\omega)$ method, that allows to compute dispersion curves for frequency-dependent problems, instead of using the $\omega(k)$ one that leads to non-linear eigenvalue problems.
Until now, this type of model has never been implemented to handle porous material models with periodic inclusions [2], [3]. This will render possible to overcome the limits of existing approaches, by a more specific design of the system through a process of optimization and testing of different inclusions, in order to obtain a device whose frequency efficiency outperforms existing designs.
Dispersion curves (calculated with the shift cell technique) and acoustical characteristics (computed using Floquet-Bloch periodic conditions) for different numerical test cases are shown. In particular, they are obtained for a 3D melamine unit cell, with and without inclusion. The behaviour of this porous material is described by JCA model in the following pages, but one can identically use any other equivalent fluid model.

2. FLOQUET-BLOCH THEORY

Floquet-Bloch (hereafter F-B) theory provides a strategy to analyse the behaviour of systems with a periodic structure. Floquet's seminal paper deals with the solution of 1D partial differential equations with periodic coefficients; in solid state physics, Bloch generalizes Floquet's results to 3D systems and obtains the description of the wave function associated with an electron traveling across a periodic crystal lattice. This wave function is a solution of the

Schrödinger equation with a periodic potential and Bloch showed that it is the product of a simple plane wave multiplied by a periodic function with the same periodicity of the lattice.
In the literature dealing with wave propagation problems in mechanical systems the theory is referred to as Floquet-Bloch theory or, simply, Floquet theory [4]. In layered systems, due to the heterogeneity of the relevant elastic properties, to particular geometric features, or to both, only certain wave modes can physically propagate inside the structure. Each of these modes can be identified by a determined (generally nonlinear) function relating the time frequency and the spatial frequency (or wave number). These relationships are called dispersion curves and they summarize all the oscillatory behaviour of the system. Dispersion curves provide estimations of the elastic and geometrical parameters from experiments or numerical models and offer a better perspective to explain the wave field behaviour inside bodies.

3. SHIFT CELL OPERATOR TECHNIQUE

Considering a porous layer as an equivalent fluid [5], the starting equation for developing the associated shift cell formulation is

$$(\nabla + j\boldsymbol{k})^T \left(\frac{1}{\rho}(\nabla + j\boldsymbol{k})\boldsymbol{p}\right) = -\frac{\omega^2}{K}\boldsymbol{p}, \tag{1}$$

with $\rho = \rho(material, \omega)$ and $K = K(material, \omega)$.
By further developing the latter equation and considering $\boldsymbol{p} = pe^{j\boldsymbol{kx}}$ where $\boldsymbol{k}$, for a 3D application (Figure 1), is

$$\boldsymbol{k} = k\boldsymbol{\phi}, \boldsymbol{\phi} = \begin{pmatrix} cos\theta cos\phi \\ cos\theta sin\phi \\ sin\theta \end{pmatrix}, \tag{2}$$

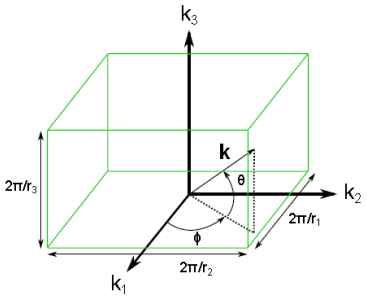

Figure 1: Reciprocal lattice vector in a 3D unitary cell [3].

one can obtain

$$\nabla^T \frac{\nabla(pe^{j\boldsymbol{kx}})}{\rho} + j\boldsymbol{k}^T \left(2\frac{\nabla(pe^{j\boldsymbol{kx}})}{\rho} + pe^{j\boldsymbol{kx}}\nabla\frac{1}{\rho}\right) - \boldsymbol{k}^T\boldsymbol{k}\frac{pe^{j\boldsymbol{kx}}}{\rho} + \frac{\omega^2}{K}pe^{j\boldsymbol{kx}} = 0. \tag{3}$$

3.1. Weak formulation

The weak formulation is calculated from the following equation, where $\tilde{p}$ is a weighting test function:

$$\int_\Omega \tilde{p}e^{-j\boldsymbol{k}^T\boldsymbol{x}} \left(\nabla^T \frac{\nabla(pe^{j\boldsymbol{kx}})}{\rho} + j\boldsymbol{k}^T \left(2\frac{\nabla(pe^{j\boldsymbol{kx}})}{\rho} + pe^{j\boldsymbol{kx}}\nabla\frac{1}{\rho}\right) - \boldsymbol{k}^T\boldsymbol{k}\frac{pe^{j\boldsymbol{kx}}}{\rho} + \frac{\omega^2}{K}pe^{j\boldsymbol{kx}}\right) d\Omega = 0 \tag{4}$$

$$\int_\Omega \left(\frac{1}{\rho}\nabla^T\tilde{p}\nabla p - j\boldsymbol{k}^T\frac{2}{\rho}(\tilde{p}\nabla p - \nabla\tilde{p}p) + \boldsymbol{k}^T\boldsymbol{k}\frac{4}{\rho}\tilde{p}p - \omega^2\frac{1}{K}\tilde{p}p\right) d\Omega = 0 \tag{5}$$

Considering that $\boldsymbol{\varphi}$ is the eigenvector, the equation can be written in its matrix form

$$(\boldsymbol{K} + jk\boldsymbol{L} + k^2\boldsymbol{H} - \omega^2\boldsymbol{M})\boldsymbol{\varphi} = 0 \tag{6}$$

with the following matrices:

- $\boldsymbol{K} \rightarrow \int_\Omega \frac{1}{\rho}\nabla\tilde{p}\nabla p\, d\Omega$;
- $\boldsymbol{L} \rightarrow \int_\Omega \frac{2}{\rho}(\nabla\tilde{p}p - \tilde{p}\nabla p)\, d\Omega$;

- $\boldsymbol{H} \rightarrow \int_{\Omega} \frac{4}{\rho} \tilde{p} p \, d\Omega$;
- $\boldsymbol{M} \rightarrow \int_{\Omega} \frac{1}{K} \tilde{p} p \, d\Omega$.

3.2. Right and left eigenvalue problems

The latter formulation leads to the following right eigenvalue problem:

$$[(\boldsymbol{K} - \omega^2 \boldsymbol{M}) + \lambda_i \boldsymbol{L} - \lambda_i^2 \boldsymbol{H}]\boldsymbol{\varphi}_i^r = 0 \tag{7}$$

where $\lambda_i = jk_i$ is the i-th eigenvalue, φ_i^r denotes the right eigenvector associated to λ_i, $\boldsymbol{M}$ and $\boldsymbol{K}$ are respectively the standard symmetric definite mass and symmetric semi-definite stiffness matrices, $\boldsymbol{L}$ is a skew-symmetric matrix and $\boldsymbol{H}$ is a symmetric semi-definite positive matrix. In this formulation, all matrices are frequency dependent.

For frequency-dependent systems, the estimation of the group velocity is not trivial. The equation (7) can be rewritten as

$$\boldsymbol{A}_1(\omega)\boldsymbol{\psi}_i^r = \lambda_i \boldsymbol{A}_2(\omega)\boldsymbol{\psi}_i^r \tag{8}$$

with

- $\boldsymbol{A}_1(\omega) = \begin{pmatrix} 0 & \boldsymbol{I_d} \\ \boldsymbol{K} - \omega^2 \boldsymbol{M} & \boldsymbol{L} \end{pmatrix}$;
- $\boldsymbol{A}_2(\omega) = \begin{pmatrix} \boldsymbol{I_d} & 0 \\ 0 & \boldsymbol{H} \end{pmatrix}$;
- $\boldsymbol{\psi}_i^r = \begin{pmatrix} \boldsymbol{\varphi}_i^r \\ \lambda_i \boldsymbol{\varphi}_i^r \end{pmatrix}$.

where $\boldsymbol{I_d}$ is the identity matrix.

Conversely, a left-eigenvector for the same eigenvalue satisfies

$$\boldsymbol{\psi}_i^{l^T} \boldsymbol{A}_1(\omega) = \lambda_i \boldsymbol{\psi}_i^{l^T} \boldsymbol{A}_2(\omega), \text{ with } \boldsymbol{\psi}_i^l = \begin{pmatrix} \boldsymbol{A} \\ \boldsymbol{B} \end{pmatrix}. \tag{9}$$

$$\begin{cases} \boldsymbol{B} = \boldsymbol{\varphi}_{-i}^r = \boldsymbol{\varphi}_i^l \\ \boldsymbol{A}^T = \lambda_i \boldsymbol{\varphi}_{-i}^{r^T} \boldsymbol{H} - \boldsymbol{\varphi}_{-i}^{r^T} \boldsymbol{L} = \lambda_i \boldsymbol{\varphi}_i^{l^T} \boldsymbol{H} - \boldsymbol{\varphi}_i^{l^T} \boldsymbol{L} \end{cases} \tag{10}$$

In the resolution of the right eigenvalue problem, the i-th mode ($i \in N^+$) is defined by its $\lambda_i \geq 0$ and its eigenvector $\boldsymbol{\varphi}_i^r$. For each mode i, a mode $-i$ is associated with $\lambda_{-i} \leq 0$ such that $\lambda_{-i} = -\lambda_i$ and $\boldsymbol{\varphi}_{-i}^r = \boldsymbol{\varphi}_i^l$. by solving the right eigenvalue problem, the left solution is found too.

The starting equation is now differentiated and multiplied by the left eigenvector such that

$$\frac{\partial \boldsymbol{A}_1(\omega)}{\partial \omega}\boldsymbol{\psi}_i^r + \boldsymbol{A}_1(\omega)\frac{\partial \boldsymbol{\psi}_i^r}{\partial \omega} = \frac{\partial \lambda_i}{\partial \omega}\boldsymbol{A}_2(\omega)\boldsymbol{\psi}_i^r + \lambda_i \frac{\partial \boldsymbol{A}_2(\omega)}{\partial \omega}\boldsymbol{\psi}_i^r + \lambda_i \boldsymbol{A}_2(\omega)\frac{\partial \boldsymbol{\psi}_i^r}{\partial \omega} \tag{11}$$

$$\boldsymbol{\psi}_i^{l^T}\frac{\partial \boldsymbol{A}_1(\omega)}{\partial \omega}\boldsymbol{\psi}_i^r + \boldsymbol{\psi}_i^{l^T}\boldsymbol{A}_1(\omega)\frac{\partial \boldsymbol{\psi}_i^r}{\partial \omega} =$$

$$= \boldsymbol{\psi}_i^{l^T}\left(\frac{\partial \lambda_i}{\partial \omega}\boldsymbol{A}_2(\omega) + \lambda_i \frac{\partial \boldsymbol{A}_2(\omega)}{\partial \omega}\right)\boldsymbol{\psi}_i^r + \boldsymbol{\psi}_i^{l^T}\lambda_i \boldsymbol{A}_2(\omega)\frac{\partial \boldsymbol{\psi}_i^r}{\partial \omega} \tag{12}$$

Considering that

$$\boldsymbol{\psi}_i^{l^T}\boldsymbol{A}_1(\omega) = \lambda_i \boldsymbol{\psi}_i^{l^T}\boldsymbol{A}_2(\omega) \tag{13}$$

one obtains

$$\frac{\partial \lambda_i}{\partial \omega} = \frac{\boldsymbol{\psi}_i^{l^T}\left[\frac{\partial \boldsymbol{A}_1(\omega)}{\partial \omega} - \lambda_i \frac{\partial \boldsymbol{A}_2(\omega)}{\partial \omega}\right]\boldsymbol{\psi}_i^r}{\boldsymbol{\psi}_i^{l^T}\boldsymbol{A}_2(\omega)\boldsymbol{\psi}_i^r} \tag{14}$$

which gives the expression of the group slowness using $\lambda_i = jk_i$:

$$\frac{\partial k_i}{\partial \omega} = -j\frac{\boldsymbol{\varphi}_i^{l^T}\left[-2\omega\boldsymbol{M} + \frac{\partial \boldsymbol{K}}{\partial \omega} + \lambda_i \frac{\partial \boldsymbol{L}}{\partial \omega} - \lambda_i^2 \frac{\partial \boldsymbol{H}}{\partial \omega}\right]\boldsymbol{\varphi}_i^r}{\boldsymbol{\varphi}_i^{l^T}[-\boldsymbol{L} + 2\lambda_i \boldsymbol{H}]\boldsymbol{\varphi}_i^r} \tag{15}$$

The group velocity is the inverse of the group slowness:

$$C_g = \frac{\partial \omega}{\partial k_i} = \frac{j\boldsymbol{\varphi}_i^{l^T}[-\boldsymbol{L} + 2\lambda_i \boldsymbol{H}]\boldsymbol{\varphi}_i^r}{\boldsymbol{\varphi}_i^{l^T}\left[-2\omega\boldsymbol{M} + \frac{\partial \boldsymbol{K}}{\partial \omega} + \lambda_i \frac{\partial \boldsymbol{L}}{\partial \omega} - \lambda_i^2 \frac{\partial \boldsymbol{H}}{\partial \omega}\right]\boldsymbol{\varphi}_i^r} \tag{16}$$

3.3. Classifying criteria to distinguish propagative and evanescent waves

Applying the shift cell operator technique to a sample modelled by an equivalent fluid, all the wave numbers are complex; consequently, there are not purely propagative solutions anymore. All waves are evanescent, with an evanescence rate that may be used to classify the branches in two categories: those that will be rapidly damped and those that will be slowly damped in space, with the latter that could be classified as propagative ones.
The distinction between the two is difficult and thus some classifying criteria are required:

- the ratio between the real and the imaginary parts of every wavenumber $\rightarrow C_1 = real(k)/imag(k)$;
- the ratio between the real and the imaginary parts of the energy transport speed $v = I/E$, where E is approximated by $E = 2E_k \rightarrow C_2 = real(v)/imag(v)$;
- the ratio between the real part and the imaginary parts of the group velocity $\rightarrow C_3 = real(C_g)/imag(C_g)$.

Note that $E_k = \frac{1}{2}mC_p{}^2$. Only the waves corresponding to $C_1 > \tau_1$, $C_2 > \tau_2$ and $C_3 > \tau_3$ are considered propagative. In practice, for the purpose of the following analysis, the thresholds τ are chosen such as $\tau_1 = \tau_2 = \tau_3 = 1$. This is an arbitrary choice and these values are not meant to be considered as universal: for each different case, one may need to tune them [3].

3.4. Validation of the method

The validation analysis is carried out in the frequency range 0 – 17000 [Hz]; this range of frequencies assures that the wavelength is much larger than the pore size, which is a necessary condition in order to use equivalent fluid models. The 2D and 3D unitary cells are respectively constituted by a 2 [cm] square with a 0.5 [cm] radius circular hole and by a 2 [cm] cube with a 0.5 [cm] radius cylindrical hole. For similar cases, some results are available in literature in terms of absorption coefficient [6].
In order to validate the implementation, a first calculation is made to compare shift cell results with those obtained using Floquet-Bloch periodic conditions, using (non-dissipative) air as material. Both methods are used to obtain the dispersion diagram along the direction that corresponds to $\phi = 0°$ and $\theta = 0°$ (for the 3D case) in the first Brillouin zone. Stepped (red) lines in Figure 2 correspond to the results obtained with the Floquet-Bloch method, while (blue) points correspond to the results obtained with the shift cell operator method. The comparison shows a perfect agreement between the results of the two methods.

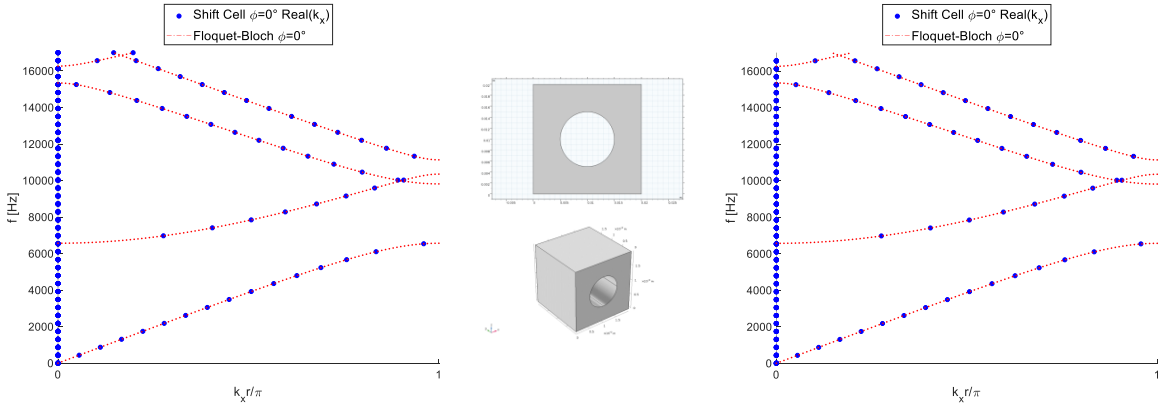

Figure 2: Comparison between dispersion curves obtained with Floquet-Bloch and shift cell techniques on a 2D (on the left) and a 3D (on the right) air unit cell.

3.5. Meaning and behaviour of band gaps for inclusions of increasing size

The imaginary part of dispersion curves is linked to dissipation, while the real part represents the propagative behaviour.
Figure 3 shows what happens to the band gap size, in the previously defined 2D unit cell, when the size of the inclusion (that has perfectly rigid walls) changes. The radius of the inclusion for the three analysed cases are respectively equal to $\frac{s}{32}$, $\frac{s}{4}$ and $\frac{s}{2.1}$, where s is the side length. After this, instead of using the adiabatic value (142 [kPa]) for the bulk modulus of air, one can artificially add a frequency-constant imaginary part to it (for example: 142+j12 [kPa]); doing so, one can simulate a band gap behaviour similar to that obtained when using equivalent fluids, as shown later. Indeed, a complex bulk modulus prevents the presence of proper band gaps in dispersion curves; one can clearly see that the gap is opening but, because of the damping, k_x is no longer purely imaginary. So, the real part of k_x does not disappear anymore, but remains low (compared to imaginary one), which means that the wave will be strongly spatially attenuated, and this is exactly the expected behaviour for band gaps in dissipative media.

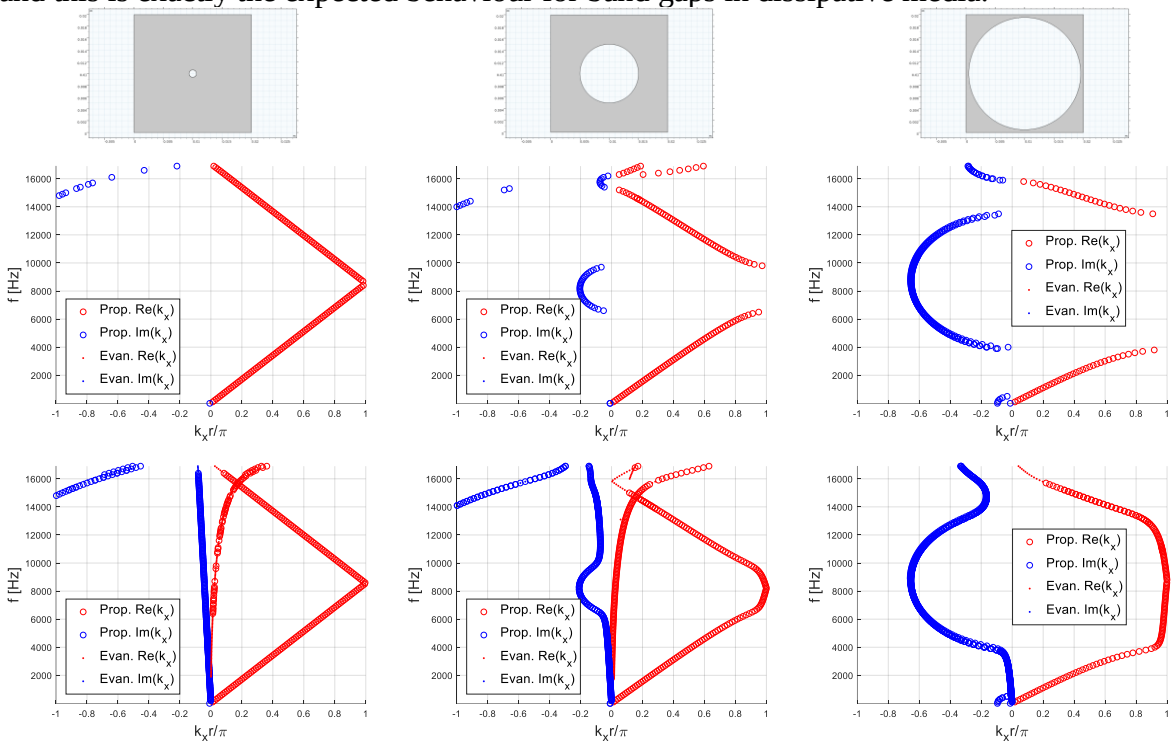

Figure 3: Dispersion curves for an air 2D cell, with increasing inclusion size (from left to right) and with normal (second raw) and modified (third raw) bulk modulus.

4. DISPERSION CURVES

For each dispersion curve plot, three eigenvectors are reported in terms of acoustic pressure field (Figures 4 and 5). Only the real parts are shown, the imaginary parts being null. They are all extracted at the frequency of 8500 [Hz] (half of the range) and along the direction that corresponds to $\theta = \phi = 0°$ in the first Brillouin zone. Their branches are ordered as: at increasing frequencies, 1st is represented by the first real part that reaches the unitary value, 2nd is the second and so on.
The fundamental acoustic parameters of the tested porous material have been experimentally determined in GAUS laboratory at University of Sherbrooke (Canada) and are: porosity $= 0.99$, tortuosity $= 1.02$, resistivity $= 8430 \left[\frac{Pa*s}{m^2}\right]$, viscous characteristic length $= 0.138\ [mm]$, thermal characteristic length $= 0.154\ [mm]$, density $= 5.73\ \left[\frac{kg}{m^3}\right]$.

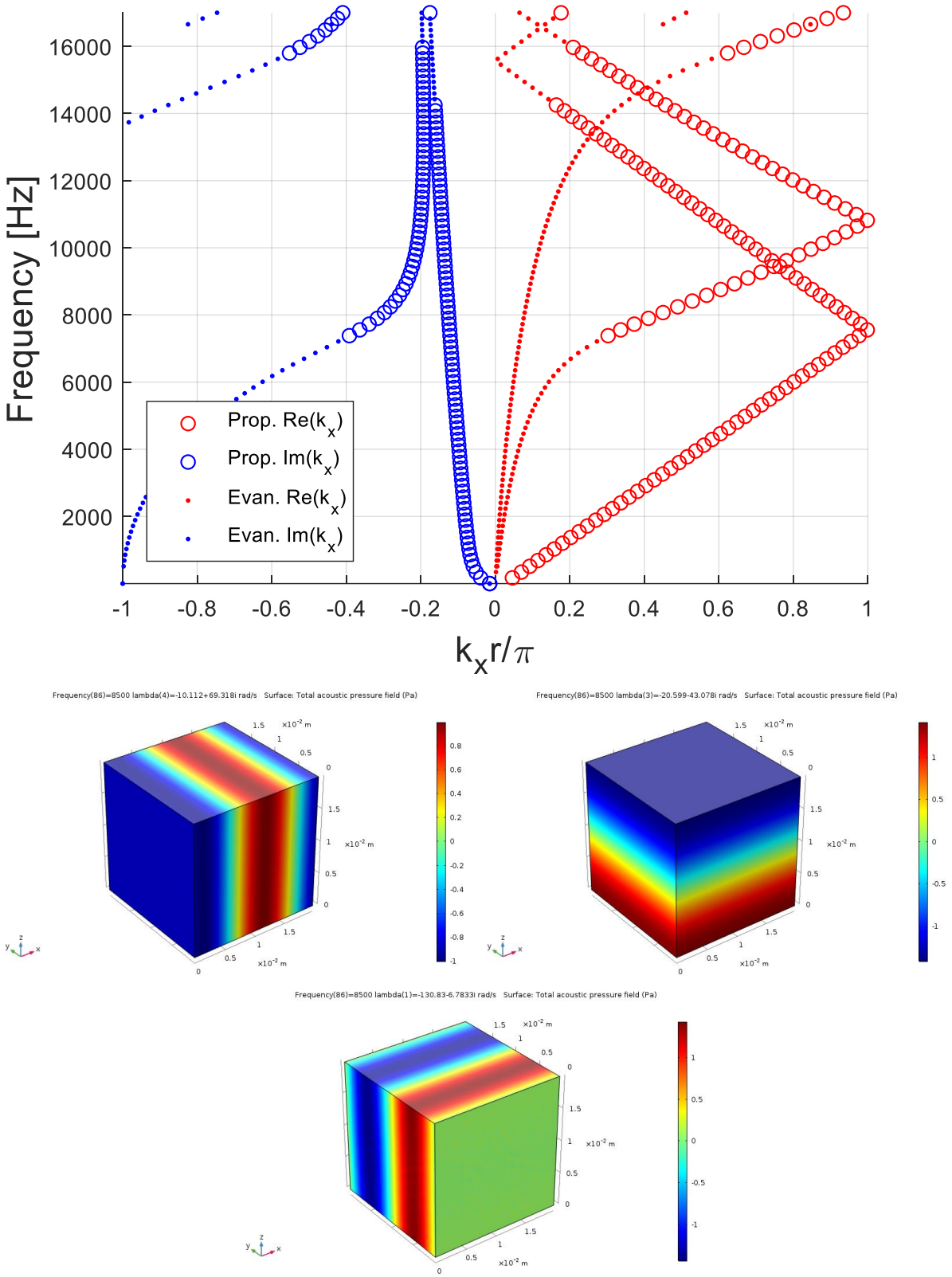

Figure 4: Dispersion curves for a homogeneous melamine unit cell and, from top left to bottom, real parts of the 1st, 2nd and 3rd branch eigenvectors.

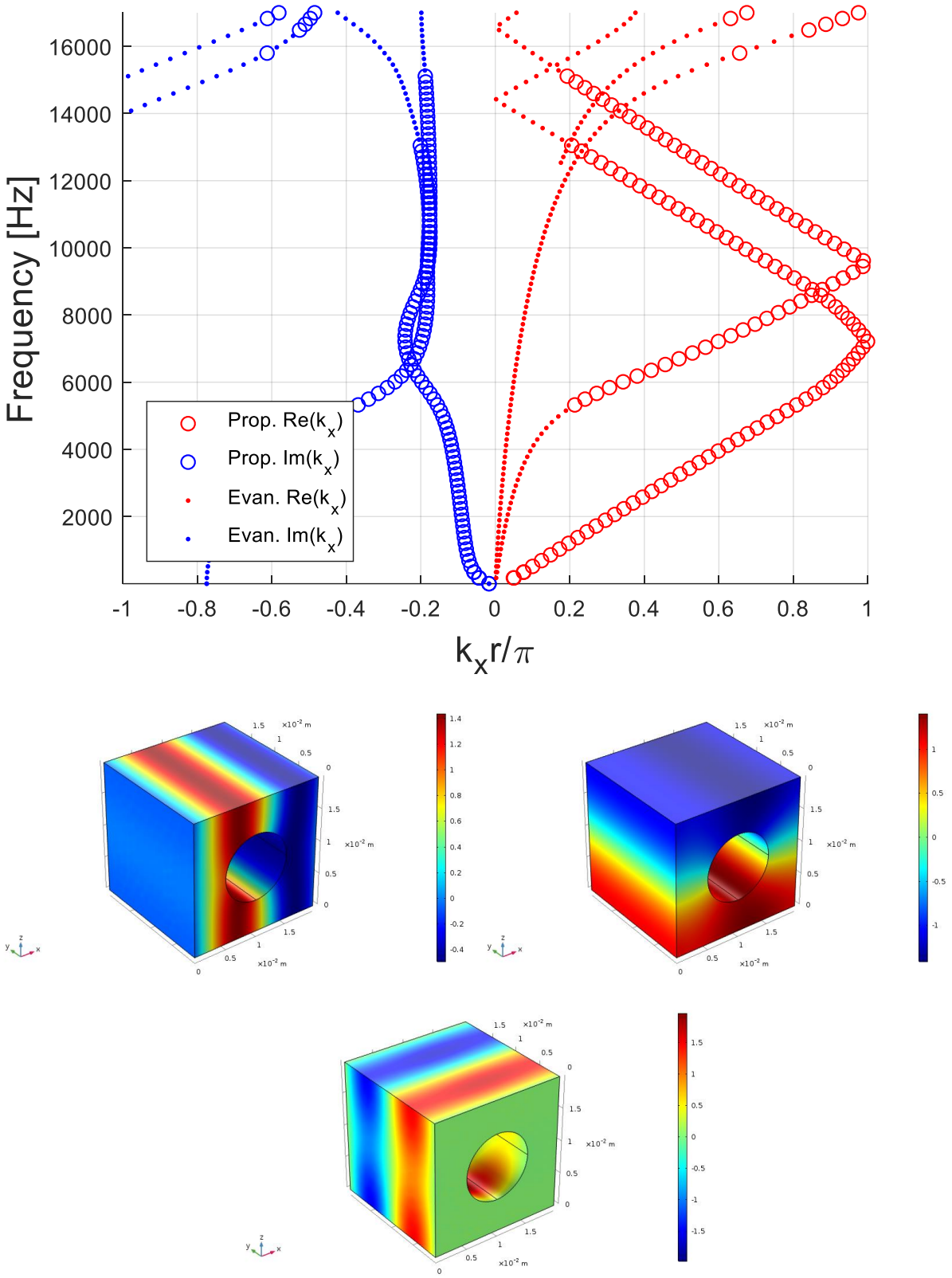

Figure 5: Dispersion curves for a melamine unit cell with inclusion and, from top left to bottom, real parts of the 1st, 2nd and 3rd branch eigenvectors.

One may notice that there are some discontinuous curves: this is probably due to the fact that, as said, all waves are evanescent with different rates: a non-perfect tuning of the sorting criteria could lead to lines that disappears and reappears on the plots.

5. TRANSMISSION LOSS

While dispersion curves are computed for an infinite repetition of unit cells, transmission loss is calculated for a finite repetition of 5 unit cells, using the same domain and boundary conditions of the infinite periodic system. This, in a first approximation, allows to compare the dispersion relations and the acoustical characteristics of the equivalent finite medium. Indeed, a further increasing in the number of repeated cells would lead to a change in the mean value of absorption coefficient and transmission loss respectively below 2% and 20% respect to the usage of a repetition of 5 unit cells.
The transmission loss is numerically computed as

$$TL = 10 \log_{10} \frac{\Pi_{incident}}{\Pi_{transmitted}} \tag{17}$$

where $\Pi_{incident}$ and $\Pi_{transmitted}$ represent the incident and transmitted power, respectively. For our plane wave configuration, the latter is compared, for homogeneous flat configurations, with the Transfer matrix method [7]:

$$TL = 10 \log \left(\frac{1}{4} \left| T_{11} + \frac{T_{12}}{\rho_0 c_0} + \rho_0 c_0 T_{21} + T_{22} \right|^2 \right), \tag{18}$$

$$\text{with} \begin{bmatrix} T_{11} & T_{12} \\ T_{21} & T_{22} \end{bmatrix} = \begin{bmatrix} \cos(kd) & j \sin(kd)\, Z_0 \\ \frac{j \sin(kd)}{Z_0} & \cos(kd) \end{bmatrix} \tag{19}$$

For the inhomogeneous configuration, the validation is obtained using an implementation of the plane wave forced response of the periodic cell accounting for fluid loading [8].

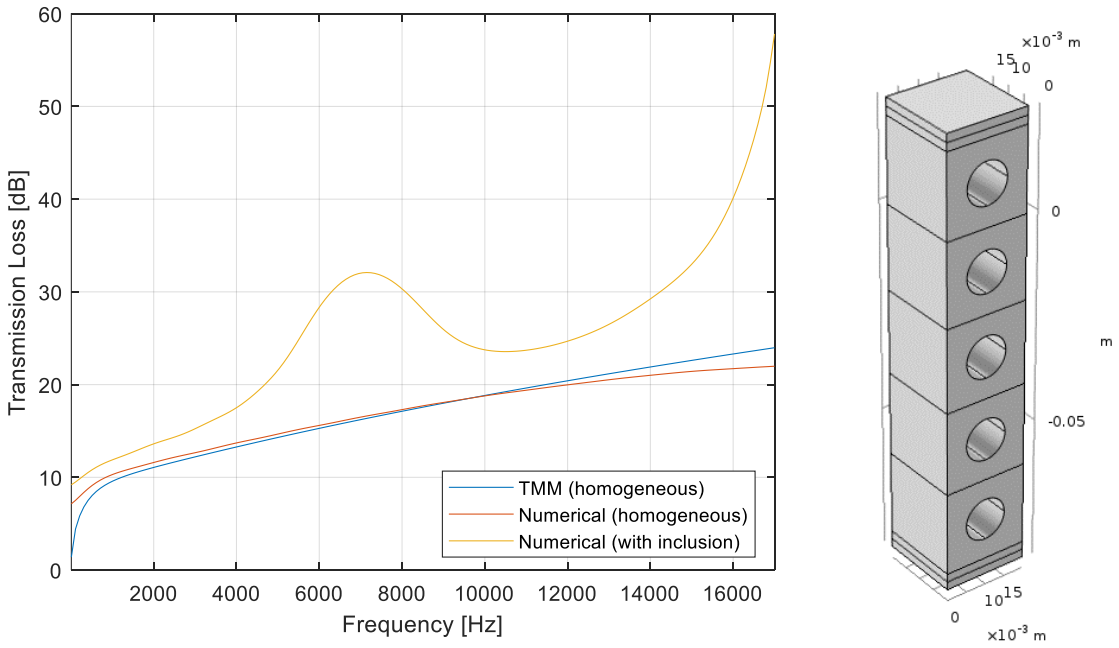

Figure 6: Transmission loss computed for a 3D repetition of 5 melamine unit cells.

Concerning the case with the inclusion, one can notice that an improvement of transmission loss properties, respect to the homogeneous case, is shown at all frequencies, in particular in correspondence of a peak at a frequency around 7 [kHz], in which it is equal to about 15 [dB], and at high frequencies. Note that, for the sake of comparison with the related dispersion curves, only their 1st branch is meaningful due to the fact that the correspondent mode is the only one

that is actually excited during these transmission loss simulations. Indeed, the improvement peak exactly corresponds to the frequency range of the 1st branch of dispersion curves in which the wave is strongly spatially attenuated.
This is definitely encouraging, for the purpose of deriving the equivalent acoustic properties of the unit cell from its dispersion characteristics.

6. CONCLUSIONS

The shift cell technique has been presented, providing details on its numerical formulation. It has been necessary to introduce some classifying criteria and, consequently, the derivation of the group velocity expression. A validation, made by a comparison with Floquet-Bloch periodic conditions, has been shown before explaining the meaning and behaviour of band gaps in dispersion curves. Dispersion curves and transmission loss plots have then been computed for a JCA-modelled melamine unit cell. Further developments of the work will include the estimation of the computational efficiency between the shift cell and the Floquet-Bloch approaches, the study of a case for actual low-frequency performance improvement and the implementation of the shift cell technique using Biot model, for both 2D and 3D geometries.

ACKNOLEDGEMENTS

This project has received funding from the European Union's Horizon 2020 research and innovation program under the Marie Skłodowska-Curie grant agreement No. 675441.

REFERENCES

[1] D. Magliacano, M. Ouisse, A. Khelif, S. De Rosa, and F. Franco, "The shifted cell operator technique applied to equivalent fluids models for the computation of dispersion diagrams of periodic porous materials," in *SAPEM 2017 proceedings*, 2017.

[2] M. Collet, M. Ouisse, M. Ruzzene, and M. N. Ichchou, "Floquet-Bloch decomposition for the computation of dispersion of two-dimensional periodic, damped mechanical systems," *Int. J. Solids Struct.*, vol. 48, no. 20, pp. 2837–2848, 2011.

[3] K. Billon, "Composites periodiques fonctionnels pour l'absorption vibroacoustique large bande," *PhD thesis Univ. Fr.*, 2017.

[4] Floquet and Gaston, "Sur les équations différentielles linéaires à coefficients périodiques," *Ann. Sci. l'École Norm. Supérieure*, vol. 12, no. Série 2, pp. 47–88, 1883.

[5] O. Doutres, Y. Salissou, N. Atalla, and R. Panneton, "Evaluation of the acoustic and non-acoustic properties of sound absorbing materials using a three-microphone impedance tube," *Appl. Acoust.*, vol. 71, no. 6, pp. 506–509, 2010.

[6] J.-P. Groby, A. Duclos, O. Dazel, L. Boeckx, and W. Lauriks, "Absorption of a rigid frame porous layer with periodic circular inclusions backed by a periodic grating.," *J. Acoust. Soc. Am.*, vol. 129, no. 5, pp. 3035–46, 2011.

[7] J. F. Allard and N. Atalla, *Propagation of Sound in Porous Media: Modelling Sound Absorbing Materials*. 2009.

[8] N. Atalla, *NOVAFEM User's guide*. Sherbrooke (QC, Canada): Université de Sherbrooke, 2017.